The Iquique earthquake sequence of April 2014: Bayesian modeling accounting for prediction uncertainty

Z. Duputel[1,2], J. Jiang[2], R. Jolivet[2,3], M. Simons[2], L. Rivera[1,2], J.-P. Ampuero[2], B. Riel[2], S. E. Owen[4], A. W. Moore[4], S. V. Samsonov[5], F. Ortega Culaciati[6], and S. E. Minson[2,7]

[1] Institut de Physique du Globe de Strasbourg, Université de Strasbourg/EOST, CNRS, Strasbourg, France, [2] Seismological Laboratory, California Institute of Technology, Pasadena, California, USA, [3] Now at Ecole Normale Supérieure, Department of Geosciences, PSL Research University, Paris, France, [4] Jet Propulsion Laboratory, California Institute of Technology, Pasadena, California, USA, [5] Canada Centre for Mapping and Earth Observation, Natural Resources Canada, Ottawa, Ontario, Canada, [6] Departamento de Geofísica, Universidad de Chile, Santiago, Chile, [7] Now at U.S. Geological Survey, Earthquake Science Center, Menlo Park, California, USA

Abstract The subduction zone in northern Chile is a well-identified seismic gap that last ruptured in 1877. On 1 April 2014, this region was struck by a large earthquake following a two week long series of foreshocks. This study combines a wide range of observations, including geodetic, tsunami, and seismic data, to produce a reliable kinematic slip model of the $M_w = 8.1$ main shock and a static slip model of the $M_w = 7.7$ aftershock. We use a novel Bayesian modeling approach that accounts for uncertainty in the Green's functions, both static and dynamic, while avoiding nonphysical regularization. The results reveal a sharp slip zone, more compact than previously thought, located downdip of the foreshock sequence and updip of high-frequency sources inferred by back-projection analysis. Both the main shock and the $M_w = 7.7$ aftershock did not rupture to the trench and left most of the seismic gap unbroken, leaving the possibility of a future large earthquake in the region.

1. Introduction

The largest historical seismic event reported in northern Chile is the great megathrust earthquake of 1877 with an estimated magnitude of 8.8 (cf., Figure 1) [*Comte and Pardo*, 1991; *Lomnitz*, 2004]. This event was preceded by the 1868 earthquake in southern Peru that ruptured southward into northern Chile (cf., Figure 1) [*Dorbath et al.*, 1990]. The relative sizes of the 1868 and 1877 events are uncertain. Local tsunami wave heights suggest that the former event is smaller, with 14 m for the 1868 earthquake in Arica (located directly onshore of the rupture) and 21 m for the 1877 event in Mejillones (located south of the faulting area; [*Abe*, 1979]). On the other hand, far-field tsunami amplitudes in Hawaii and San Francisco are similar for the two earthquakes (around 5 m at Hilo for both events, 0.2 m and 0.3 m at San Francisco in 1868 and 1877, respectively; [*Iida et al.*, 1967]) but are associated with less direct travel paths for the 1868 event, which suggest that this event may be larger than the 1877 earthquake. More recently, the 2001 $M_w = 8.4$ Arequipa earthquake partially reruptured the 1868 rupture zone and the 2007 $M_w = 7.7$ Tocopilla earthquake broke the southern downdip segment of the 1877 faulting area [*Pritchard et al.*, 2006, 2007; *Béjar-Pizarro et al.*, 2010]. The remaining unbroken ~600 km long region shown in Figure 1 may have accumulated about 9 m of slip deficit since 1868/1877 and has been identified as the North Chilean or Iquique seismic gap [*Kelleher*, 1972; *Nishenko*, 1991; *Metois et al.*, 2013]. Although very little is known about previous historical events, large earthquakes in northern Chile were reported in 1615 and 1768 and in southern Peru in 1604 and 1784, corresponding to an average recurrence interval of about 130 years over the entire gap.

On 1 April 2014, northern Chile experienced a great earthquake which ruptured the central portion of the 1868/1877 seismic gap (23:46:45 UTC, epicenter 19.572°S, 70.908°W [National Seismological Center of Chile (CSN)]). This event was preceded by an intense foreshock sequence [*Brodsky and Lay*, 2014] and followed by a large $M_w = 7.7$ aftershock. W phase inversion [*Duputel et al.*, 2012] was performed for the $M_w = 8.1$ main shock and $M_w = 7.7$ aftershock (Figure S1, available in the supporting information). The point source solutions shown in Figure 1 are similar to those found in the Global Centroid Moment Tensor (GCMT) catalog. Several coseismic slip models have been proposed for the main shock using teleseismic observations [*Yagi et al.*, 2014;
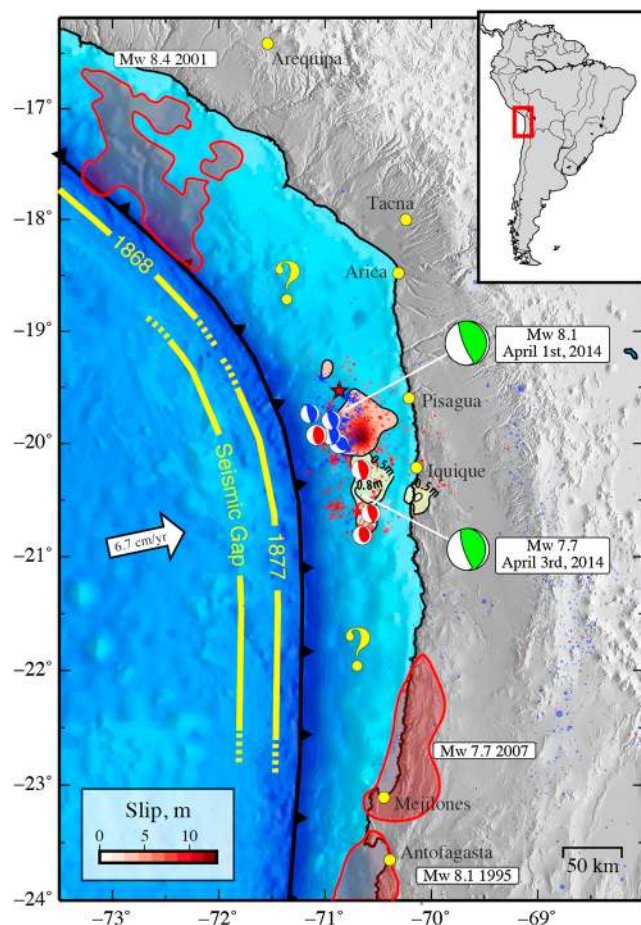
Figure 1. The 2014 Iquique earthquake sequence. Green focal mechanisms are W-phase solutions for the $M_w = 8.2$ main shock and $M_w = 7.7$ aftershock. Yellow lines indicate the supposed rupture zones for the 1868 and 1877 earthquakes [*Comte and Pardo*, 1991]. Red contours are area of ruptures of the 1995 $M_w = 8.1$ Antofagasta, the 2001 $M_w = 8.4$ Arequipa, and the 2007 $M_w = 7.7$ Tocopilla earthquakes [*Pritchard et al.*, 2006, 2007; *Béjar-Pizarro et al.*, 2010]. Black contours and red color scale indicate the preferred coseismic slip model of the main shock. Yellow filled areas present the posterior slip model obtained for the $M_w = 7.7$ aftershock. Blue and red focal mechanisms are respectively GCMT solutions for foreshocks and aftershock of $M_w > 6$ (1 January 2014 to 4 February 2014 and 1 April 2014 to 9 April 2014). Blue and red circles are respectively foreshocks and aftershocks of magnitude $4 < M < 6$ from the CSN catalog (1 January 2014 to 4 February 2014 and 1 April 2014 to 9 April 2014).

Ruiz et al., 2014], GPS static data, tsunami records [*An et al.*, 2014], or a combination of these observations [*Hayes et al.*, 2014; *Schurr et al.*, 2014; *Gusman et al.*, 2015; *Lay et al.*, 2014; *Liu et al.*, 2015]. These models show similar first-order features but also significant differences such as the amplitude, extent, location, and updip limit of the primary slip zone (cf., Figure S2). Such discrepancies complicate the interpretation of the Iquique sequence in the context of the entire earthquake cycle and limit any quantitative conclusion on the reduction of the accumulated slip deficit. These discrepancies also blur the relations between coseismic slip, high-frequency radiation, and foreshock activity [*Meng et al.*, 2015].

Going forward, we need a robust coseismic slip model to understand its spatial relationship to interseismic, preseismic, and postseismic slip, which will provide better insights into the mechanical behavior of the megathrust. With this purpose we combine a wide range of observations including interferometric synthetic aperture radar (InSAR), static GPS, tsunami, tide gauges, high-rate GPS, and strong motion data. The 2014 Iquique earthquake is investigated using an innovative Bayesian approach accounting for uncertainty in the Green's functions. Our goal is not only to obtain a trustworthy slip distribution but also to produce realistic estimates of uncertainty, which can impact our interpretation of the rupture process. We are currently working on Bayesian modeling of interseismic and postseismic deformation, which is left to a future publication.
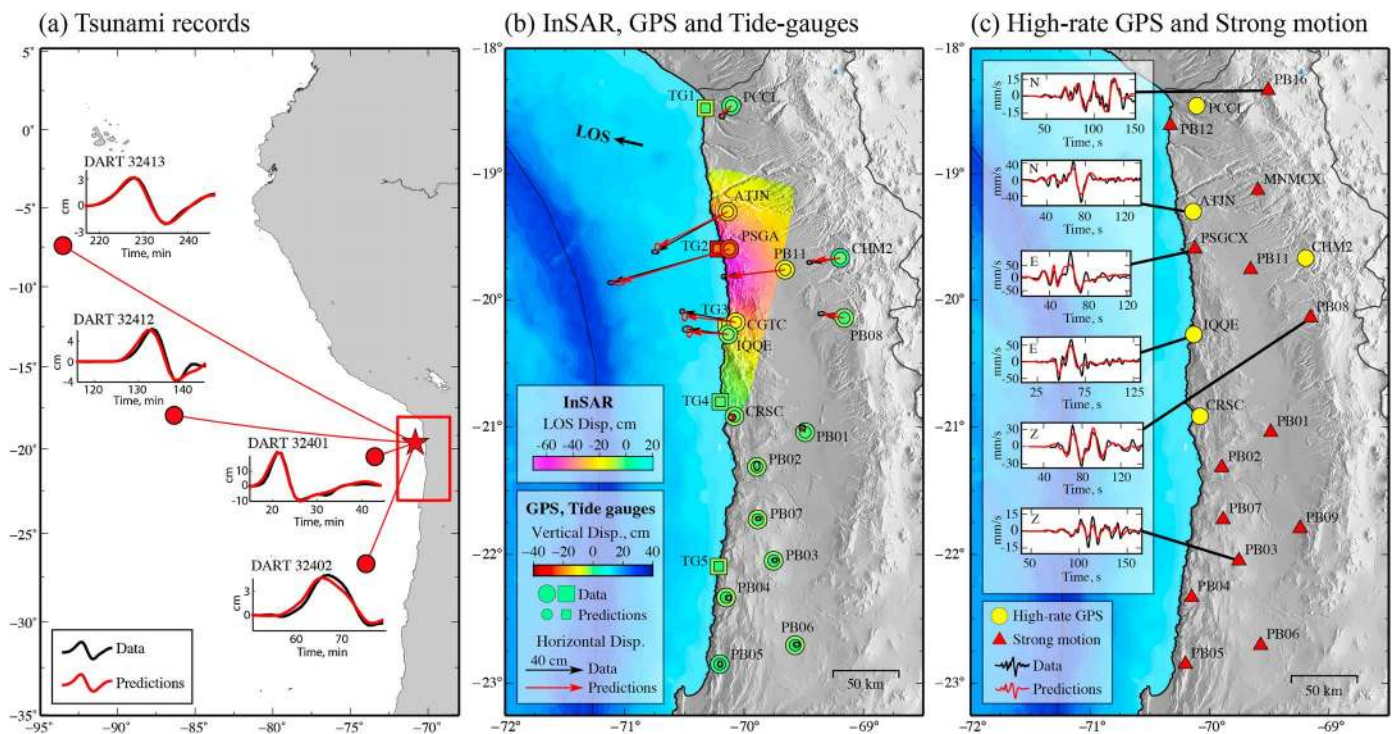
Figure 2. Geodetic, tsunami, and seismic observations. Observations are shown in black and predictions for the posterior mean model in Figure 3b are shown in red. (a) Tsunami waveforms. Red star is the Iquique main shock epicenter and red circles indicate the location of DART stations. Red box indicates the region covered in Figures 2b and 2c. (b) Geodetic data. Vectors indicate observed and predicted horizontal GPS displacements with their associated 1 σ data and prediction error ellipses. Colored circles and squares are observed (outer circles/squares) and predicted (inner circles/squares) vertical displacements from GPS and tide gauges, respectively. Dark arrows indicate line of sight direction (LOS) from the satellite to the ground. (c) High-rate GPS and strong motion data. Examples of observed waveforms (black lines) and the corresponding predictions (red lines) are presented.

2. Observations and Probabilistic Analysis

Exploiting the many different data types available in Chile, we gathered one of the most comprehensive data set to date for the 2014 Iquique earthquake (Figure 2). For joint static-kinematic modeling of the main shock, we use RADARSAT-2 InSAR data and GPS data from a network operated by the California Institute of Technology (Caltech), École Normale Supérieure (ENS), Geo Forschungs Zentrum (GFZ), and Universidad de Chile (DGF). We also measured vertical coseismic offsets using five coastal tide gauges close to the main shock epicentral area (data provided by the Servicio Hidrográfico y Oceanográfico de la Armada - SHOA). In addition, we use far-field tsunami records from Deep-ocean Assessment and Reporting of Tsunamis (DART) buoys 32401, 32402, 32412, and 32413 (cf., Figure 2). To constrain the rupture kinematics, we include near-field high-rate GPS (hrGPS) as well as strong motion data from the IPOC network [*Witze*, 2014]. We also conduct static slip modeling of the $M_w = 7.7$ aftershock using GPS, tide gauges, and tsunami data. As specified in the supporting information, we use this model to remove the aftershock signal from InSAR data before inverting the $M_w = 8.1$ main shock. Further details on data processing and modeling of the aftershock can be found in the supporting information.

Our model adopts a curved fault geometry that accounts for dip variation of the slab interface as a function of depth (cf., supporting information and Figure S5). On each fault patch we solve for the along-strike and along-dip components of slip as well as the rise time and rupture velocity. We also solve for epicenter coordinates. Each point on the fault is allowed to rupture only once during the earthquake, assuming a prescribed triangular source time function. The inversion includes additional "nuisance" parameters to account for InSAR residual orbital errors (i.e., a linear function of range and azimuth).

The inversion accounts for uncertainty in the Green's functions while also avoiding nonphysical spatial smoothing over the slip distribution. We use a Bayesian approach to derive the posterior probability density function, $p(\mathbf{m}|\mathbf{d})$, describing the full ensemble of plausible slip models, $\mathbf{m}$, that explain observations, $\mathbf{d}$, and agree with a priori assumptions, $p(\mathbf{m})$. As detailed in the supporting information, prior assumptions are

as follows: (1) no back slip in excess of 1 m and a maximum slip of 20 m, (2) a centered Gaussian prior on the strike-slip component with a standard deviation of 3 m, and (3) broad uniform prior probability density functions (PDFs) for the slip duration and rupture velocity (Figure S7). We do not use any spatial smoothing or norm damping that might bias slip inversion results [*Causse et al.*, 2010]. We have also developed a realistic error model combining measurement uncertainties and prediction errors due to Earth model inaccuracies (cf., supporting information). We use the stochastic forward model approach of *Duputel et al.* [2014] to map uncertainties in the elastic parameters into the static and kinematic predictions. Based on previous tomographic models of the region [*Legrand et al.*, 2007; *Lüth*, 2000; *Husen et al.*, 1999], we calculate the Green's functions for a reference 1-D elastic structure and estimate the error on those Green's functions assuming 5% to 20% uncertainty (cf., supporting information and Figure S6). As noted by *Jolivet et al.* [2015], ignoring the prediction error leads to biased results and overoptimistic uncertainties on the estimated slip distribution. To our knowledge, it is the first time that epistemic uncertainties in kinematic predictions are estimated using such a physically based approach. This study assumes that static ($\mathbf{d}_s$) and kinematic ($\mathbf{d}_k$) data sets are independent. If we think in the frequency domain, the physical independence between $\mathbf{d}_s$ and $\mathbf{d}_k$ is supported by the fact that kinematic data is band-passed (i.e., static displacements are removed from kinematic data). Under this assumption, data and prediction covariances still include off-diagonal components describing spatial and temporal correlations due to prediction uncertainties. The independence of $\mathbf{d}_s$ and $\mathbf{d}_k$ also enables a progressive integration of information from static and kinematic data sets.

As described in *Minson et al.* [2013], we employ a two-step approach in which we first sample for the static slip distribution

$$p(\mathbf{m}_s|\mathbf{d}_s) \propto p(\mathbf{d}_s|\mathbf{m}_s) \, p(\mathbf{m}_s) \tag{1}$$

where $\mathbf{d}_s$ represents InSAR, GPS, tide gauges, and tsunami data, and $\mathbf{m}_s$ is the vector of static slip (i.e., final, integrated slip) and nuisance parameters. Solving first for $p(\mathbf{m}_s|\mathbf{d}_s)$ allows us to shrink the sampled space before addressing the full joint kinematic rupture model

$$p(\mathbf{m}|\mathbf{d}) = p(\mathbf{m}_s, \mathbf{m}_k|\mathbf{d}_s, \mathbf{d}_k) \tag{2}$$

$$\propto p(\mathbf{d}_k|\mathbf{m}_s, \mathbf{m}_k) \, p(\mathbf{m}_s|\mathbf{d}_s) \, p(\mathbf{m}_k) \tag{3}$$

where $\mathbf{d}_k$ includes hrGPS and strong motion data and $\mathbf{m}_k$ is the vector of kinematic parameters consisting of slip duration, rupture velocity, and epicenter coordinates.

Sampling $p(\mathbf{m}|\mathbf{d})$ in a high-dimensional space is computationally challenging and has long been intractable for kinematic finite-fault source inversions. As the volume of the model space grows exponentially with its dimensionality, we have to generate a large number of samples and perform a large number of forward evaluations, a phenomenon often referred to as the *curse of dimensionality* [*Bellman*, 1961]. To tackle this problem, we use the AlTar algorithm, a parallel Markov Chain Monte Carlo (MCMC) sampler named in honor of Albert Tarantola, which exploits novel massively parallel computational approaches using Graphic Processing Units (GPUs). AlTar is based on the Cascading Adaptive Transitional Metropolis In Parallel (CATMIP) algorithm [*Minson et al.*, 2013] and includes the approach of *Duputel et al.* [2014] to account for prediction uncertainties.

3. Rupture Process of the April 2014 Earthquake Sequence

3.1. Joint Static-Kinematic Modeling of the M_w = 8.1 Main Shock

For the main shock, we sample the high-dimensional model space with a large number of samples (∼16 billion models, using 140,000 MCMC chains, the computation takes around 24 h using 90 GPUs). Figure 3 shows the mean of the posterior model ensemble and the associated uncertainty after static inversion and joint kinematic-static inversion. Comparisons between observations and predictions from the mean of the posterior model ensemble presented in Figures 2 and S8–S11 indicate good agreement for geodetic, tsunami, and seismic data.

Both static-only and joint kinematic models (Figure 3) show a primary slip zone located south of the hypocenter with a small amount of slip at shallow depth. Due to rupture time information provided by hrGPS and strong motion data, the final slip model appears sharper than the one based only on geodetic and tsunami data. The seismic moment is estimated as 1.6×10^{21} N m (M_w = 8.1), in agreement with our W phase solution.
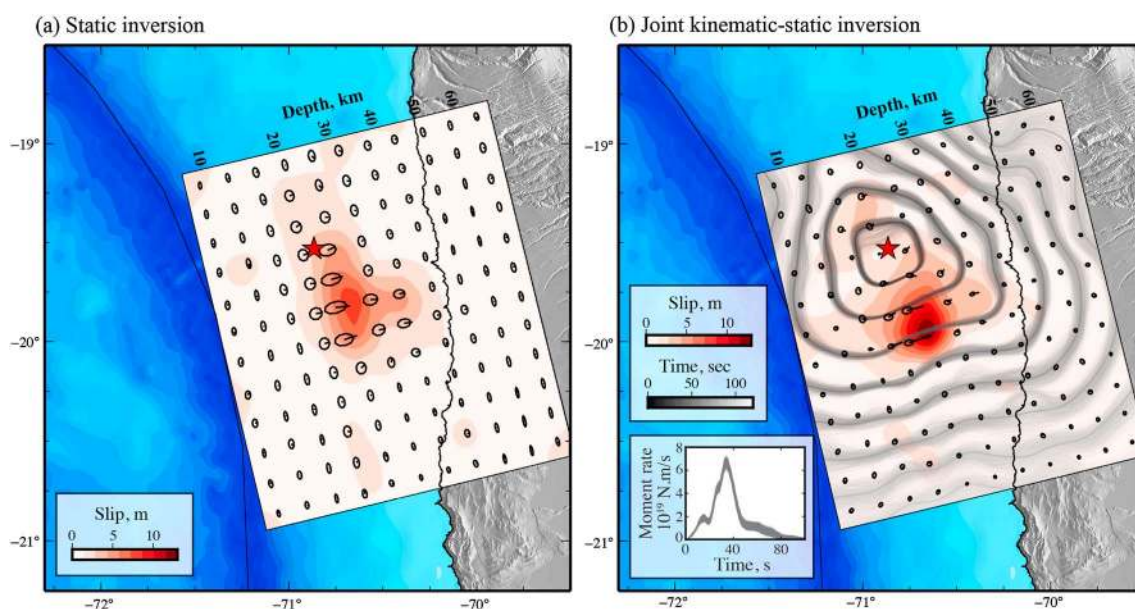
Figure 3. Probabilistic slip model obtained for the 2014 Iquique earthquake. The mean of the posterior PDF is shown (a) after static inversion and (b) after joint kinematic-static inversion. Red colors indicate slip amplitude. Arrows and their associated 95% error ellipses indicate the slip direction and uncertainty. Red star is the inverted hypocenter location. Gray lines are a posterior set of 1000 rupture fronts shown every 10 s. Bottom left inset shows the posterior ensemble of moment rate functions.

The inverted hypocenter, indicated by the red star, is consistent with the CSN hypocenter and about 15 km north of the USGS hypocenter (cf., Figure S12). Model uncertainties in Figure 3b show that the rupture front is well constrained between the hypocenter and the main asperity but poorly resolved in late stages of the rupture associated with low slip amplitudes. These late stages also show significant rupture complexity in back-projection imaging [*Meng et al.*, 2015], including rerupturing episodes that cannot be represented by the source parameterization adopted here. We also present the posterior ensemble of moment rate functions in the bottom left inset of Figure 3b. As reported previously [e.g., *Lay et al.*, 2014], there is a ~20 s interval of low moment rate at the onset of this event, corresponding to the period of time when slip propagates from the hypocenter to the primary asperity. This very slow initiation is then followed by a rapid increase of the moment rate up to 6.8×10^{19} N m/s around 35 s after the origin time.

The absence of shallow slip in our models differs from results of *Schurr et al.* [2014], *Yagi et al.* [2014], and *Liu et al.* [2015] based on seismic and geodetic data but are somewhat similar to the results of *An et al.* [2014] and *Gusman et al.* [2015], which have incorporated tsunami observations in their analysis. To assess the relative influence of each data set on different parts of the slip model, we use the sensitivity $\mathbf{S}(\mathcal{D})$, defined as

$$\mathbf{S}(\mathcal{D}) = \mathrm{diag}\left(\mathbf{G}^t(\mathcal{D}) \cdot \mathbf{C}_\chi^{-1}(\mathcal{D}) \cdot \mathbf{G}(\mathcal{D})\right) \qquad (4)$$

where $\mathbf{G}(\mathcal{D})$ and $\mathbf{C}_\chi(\mathcal{D})$ are, respectively, the Green's function for the dip slip component and covariance matrix for a given data set $\mathcal{D}$ (i.e., geodetic, tsunami or seismic data). The sensitivity plots in Figure S13 clearly show that shallow slip is well constrained by tsunami data in contrast to other data sets. Increasing the amount of slip at shallow depth produces early tsunami arrivals which are not consistent with observed waveforms. On the other hand, previous finite-fault models shown in Figure S2 depict significant slip in the downdip part of the megathrust compared to our results. As mentioned by *Hayes et al.* [2014] (cf., extended data Figure 3), downdip slip does not match InSAR data that favor slip concentrated farther away from the coast. This is also consistent with Figure S13d, showing that the downdip part is well constrained by geodetic data.

After joint inversion the near-field geodetic, tsunami, and seismic data resolve a compact slip zone located ~40 km south of the hypocenter, with maximum slip above 10 m. As shown in Figure S2, this primary slip region is more compact and has larger slip amplitude than most previously published results [e.g., *Schurr et al.*, 2014; *Lay et al.*, 2014; *An et al.*, 2014; *Yagi et al.*, 2014; *Gusman et al.*, 2015]. This difference is probably due to the imposed spatial smoothing in previous slip models, which is absent in our approach. Moreover,
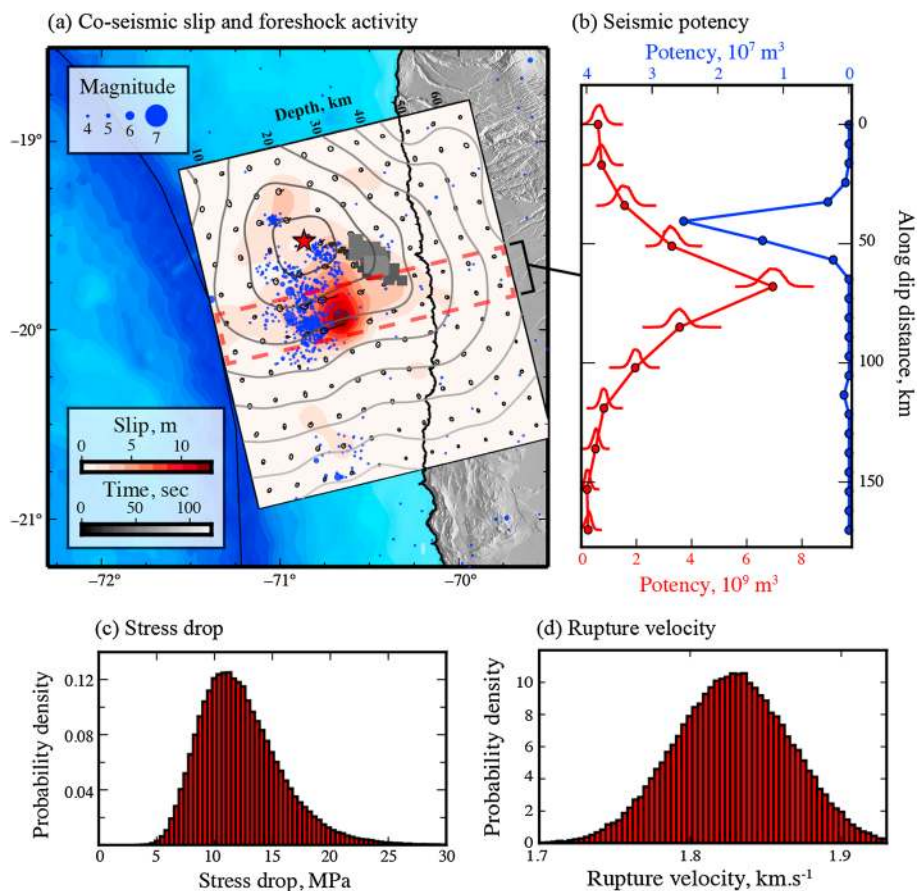
Figure 4. Spatiotemporal distribution of coseismic slip. (a) Comparison of the foreshock activity with the posterior slip model shown in Figure 3b. Gray squares are the high-frequency back projection results of *Meng et al.* [2015] scaled by beamforming amplitude. Blue circles indicate foreshock epicenters from the CSN catalog scaled by magnitude. The rectangular area marked with red dashed lines indicates the profile used for seismic potency estimates in FIgure 4b. (b) Distribution of seismic potency as a function of the along-dip distance from the trench. Red histograms and red line show the seismic potency profile estimated from our probabilistic model. Blue line shows the cumulative seismic potency of foreshocks in distance bins. (c) Posterior PDF of the average stress drop. (d) Posterior PDF of the average rupture velocity between the hypocenter and the primary slip zone located ~40 km south of the hypocenter.

additional data sets included in our analysis ensure better constraints in the inversion process. Results of *Liu et al.* [2015] and geodetic fault modeling by *Hayes et al.* [2014] also depict a compact main shock rupture but these models involve shallow slip, which is inconsistent with tsunami observations (as discussed above). The average slip for subfaults with moment at least 15% of the peak subfault moment is about 5 m. The posterior PDF of average stress drop ($\Delta\sigma$) obtained by calculating the coseismic change in shear traction at the center of each fault patch is shown in Figure 4c (cf., supporting information). This measurement is consistent with the energy-based averaging of stress drop proposed by *Noda et al.* [2013]. Although the posterior uncertainty on $\Delta\sigma$ is relatively large, the average value of 10 MPa suggests a more compact source than a 3 MPa global average [*Allmann and Shearer*, 2009]. However, for heterogeneous stress drop distribution, we expect that measurements of *Allmann and Shearer* [2009] for a circular crack model underestimates our energy-based averaging of $\Delta\sigma$ [cf., *Noda et al.*, 2013].

3.2. Static Modeling of the $M_w = 7.7$ Aftershock

The 3 April 2014 $M_w = 7.7$ aftershock is modeled using AlTar in order to draw ~1 billion models out of the posterior PDF. The mean and variability of this posterior ensemble of models are presented in Figures 1 and S14. Comparison between observations and predictions for GPS, tide gauges, and tsunami data is shown in Figures S14a and S14b.

Most of the $M_w = 7.7$ aftershock slip is located at depth larger than 20 km. As for the main shock, tsunami data is useful to constrain the absence of slip close to the trench. The aftershock is associated with two main

slip asperities near the south easternmost extent of the $M_w = 8.2$ rupture. This feature is consistent with the slip model of *Liu et al.* [2015] and the two groups of high-frequency sources reported by *Meng et al.* [2015].

Although our model matches geodetic and tsunami observations reasonably well, posterior slip uncertainty is quite large (cf., Figure S14), which prevents more detailed interpretation of the rupture process. Incorporating kinematic data to improve model resolution is left to a future study.

4. Discussion and Conclusion

The $M_w = 8.1$ Iquique earthquake shows an unusual initiation phase with very small moment rate in the first 20 s. As shown in Figure 4a, this initial phase occurred in a region where a relatively large number of foreshocks occurred. The southward rupture propagated initially with a low-average velocity (∼1.8 km/s, Figures 4d and S15) and concentrated at the edge of a large slip patch that ruptured subsequently. The foreshock activity is also concentrated in the updip periphery of this main asperity. Figure 4b illustrates this by juxtaposing the distribution of seismic potency from our probabilistic coseismic models (in red) and the cumulative seismic potency of foreshocks (in blue). As discussed previously [*Lay et al.*, 2014; *Meng et al.*, 2015], the foreshock activity may be driven by an extended slow slip event, similar to one inferred to have preceded the 2011 $M_w = 9$ Tohoku-oki earthquake [*Kato et al.*, 2012].

The initial slow rise of the moment rate function and the low rupture speed between the hypocenter and the main asperity suggest that the area around the hypocenter is associated with low stress level and high fracture energy. This interpretation is consistent with a precursory slow slip event which might have kept a low stress level in this region. The clear separation between foreshocks and coseismic slip suggests that this possible slow slip transient occurred updip of the main rupture zone and in the area where the main shock rupture was triggered. *Bouchon et al.* [2013] recently suggested that nearly 70% of large interplate earthquakes are preceded by foreshock sequences, possibly triggered by slow slip events. A preseismic transient detected on GPS stations near Pisagua has been conjectured [*Ruiz et al.*, 2014], but it may be associated mainly with the cumulative coseismic displacement of the foreshocks [*Schurr et al.*, 2014]. The amplitude of any purported preseismic creep may simply be too small to be detected by GPS stations. An alternative interpretation can be the cascade triggering of neighboring earthquakes due to static stress transfer and/or the drive of afterslip, ultimately leading to the triggering of the main shock [*Helmstetter and Sornette*, 2003].

The fast rupture speed corridor along the downdip edge of the main asperity coincides nicely with back-projection results of *Meng et al.* [2015], shown by the gray squares in Figure 4a. This distribution of high-frequency sources along the edge of the primary slip zone was observed for several previous earthquakes [*Meng et al.*, 2011; *Lay et al.*, 2012] and might be related to the presence of deep asperities [*Huang et al.*, 2012]. The back-projection showed repeated rupture along that corridor with initial rupture times that are consistent with those inferred here. These late high-frequency rupture episodes may have been induced by the relatively late rupture of the main slip asperity. However, this interpretation is uncertain because our source inversion procedure does not explicitly solve for episodes of rerupture.

Our results indicate a very localized main shock rupture with large slip, suggesting the possibility of nearly complete stress drop in a small portion of the North Chilean seismic gap. The compactness of the source differs from previously published smoothed slip models for which the main shock only reduced part of the accumulated slip deficit in the ruptured region [e.g., *Schurr et al.*, 2014; *Yagi et al.*, 2014]. Even though the April 2014 main shock involved large coseismic slip, it only ruptured a relatively small area (∼100 × 50 km) and has not released most of the interseismic strain accumulated since the 1868 and 1877 events. The fact that the rupture did not propagate further south might be related to the presence of a region of low interseismic coupling identified by several studies [*Metois et al.*, 2013; *Schurr et al.*, 2014; *Li et al.*, 2015], which could behave as a barrier to earthquake slip propagation. With a northern extent close to the southern end of the main shock rupture, the $M_w = 7.7$ aftershock partially ruptured the segment south of this low coupled barrier. As suggested by *Hayes et al.* [2014], this region was probably loaded by the main shock and the first 27 h of aftershocks. The physical relationship between the $M_w = 7.7$ aftershock and the main shock need to be further explored with improved resolution of the aftershock model and the development of a reliable postseismic model.

Our modeling results clearly show that the $M_w = 8.1$ main shock and the $M_w = 7.7$ aftershock did not rupture up to the trench. This lack of shallow slip is similar to that inferred for 1995 Antofagasta and 2007 Tocopilla

earthquakes [*Pritchard et al.*, 2006; *Béjar-Pizarro et al.*, 2010; *Motagh et al.*, 2010]. It is not obvious whether the shallow part of the megathrust interface is seismogenic. Recent geodetic studies lead to diverging conclusions about the degree of interseismic coupling at depth shallower than 30 km [*Chlieh et al.*, 2011; *Béjar-Pizarro et al.*, 2013; *Schurr et al.*, 2014; *Metois et al.*, 2013; *Li et al.*, 2015]. Using land-based geodetic data, it is very difficult to infer locking properties far offshore: because of limited resolution, small differences in modeling and smoothing approaches may result in very different coupling models. On the other hand, seafloor deformation observations off the coast of Peru suggest strong coupling at shallow depth [*Gagnon et al.*, 2005]. Whether the shallow portions of the seismic gap are coupled or not, failure in a single large event is certainly possible, as seems to have occurred in the 1868 and 1877 events. During such events, shallow slip could be encouraged by strong dynamic effects or favorable fault weakening properties [e.g., *Kozdon and Dunham*, 2013; *Noda and Lapusta*, 2013], a scenario similar to what was observed in Japan during the 2011 Tohoku-oki earthquake. As in many subduction zones, improved inland and seafloor observational networks as well as tools allowing proper posterior uncertainty estimates are necessary to better understand the relative role of seismic and aseismic processes in present day deformation.

References

Abe, K. (1979), Size of great earthquakes of 1837–1974 inferred from tsunami data, *J. Geophys. Res.*, *84*, 1561–1568.

Allmann, B. P., and P. M. Shearer (2009), Global variations of stress drop for moderate to large earthquakes, *J. Geophys. Res.*, *114*, B01310, doi:10.1029/2008JB005821.

An, C., I. Sepúlveda, and P. L. F. Liu (2014), Tsunami source and its validation of the 2014 Iquique, Chile, earthquake, *Geophys. Res. Lett.*, *41*, 3988–3994, doi:10.1002/2014GL060567.

Béjar-Pizarro, M., et al. (2010), Asperities and barriers on the seismogenic zone in North Chile: State-of-the-art after the 2007 M_W 7.7 Tocopilla earthquake inferred by GPS and InSAR data, *Geophys. J. Int.*, *183*(1), 390–406.

Béjar-Pizarro, M., A. Socquet, R. Armijo, D. Carrizo, J. Genrich, and M. Simons (2013), Andean structural control on interseismic coupling in the North Chile subduction zone, *Nat. Geosci.*, *6*(6), 462–467.

Bellman, R. (1961), *Adaptive Control Processes: A Guided Tour*, Princeton Univ. Press Princeton, N. J.

Bouchon, M., V. Durand, D. Marsan, H. Karabulut, and J. Schmittbuhl (2013), The long precursory phase of most large interplate earthquakes, *Nat. Geosci.*, *6*(4), 299–302.

Brodsky, E. E., and T. Lay (2014), Recognizing foreshocks from the 1 April 2014 Chile earthquake, *Science*, *344*(6185), 700–702.

Causse, M., F. Cotton, and P. M. Mai (2010), Constraining the roughness degree of slip heterogeneity, *J. Geophys. Res.*, *115*, B05304, doi:10.1029/2009JB006747.

Chlieh, M., H. Perfettini, H. Tavera, J.-P. Avouac, D. Remy, J.-M. Nocquet, F. Rolandone, F. Bondoux, G. Gabalda, and S. Bonvalot (2011), Interseismic coupling and seismic potential along the Central Andes subduction zone, *J. Geophys. Res.*, *116*, B12405, doi:10.1029/2010JB008166.

Comte, D., and M. Pardo (1991), Reappraisal of great historical earthquakes in the northern Chile and southern Peru seismic gaps, *Nat. Hazards*, *4*(1), 23–44.

Dorbath, L., A. Cisternas, and C. Dorbath (1990), Assessment of the size of large and great historical earthquakes in Peru, *Bull. Seismol. Soc. Am.*, *80*(3), 551–576.

Duputel, Z., L. Rivera, H. Kanamori, and G. Hayes (2012), W phase source inversion for moderate to large earthquakes (1990–2010), *Geophys. J. Int.*, *189*(2), 1125–1147.

Duputel, Z., P. S. Agram, M. Simons, S. E. Minson, and J. L. Beck (2014), Accounting for prediction uncertainty when inferring subsurface fault slip, *Geophys. J. Int.*, *197*(1), 464–482.

Gagnon, K., C. D. Chadwell, and E. Norabuena (2005), Measuring the onset of locking in the Peru–Chile trench with GPS and acoustic measurements, *Nature*, *434*(7030), 205–208.

Gusman, A. R., S. Murotani, K. Satake, M. Heidarzadeh, E. Gunawan, S. Watada, and B. Schurr (2015), Fault slip distribution of the 2014 Iquique, Chile, earthquake estimated from ocean-wide tsunami waveforms and GPS data, *Geophys. Res. Lett.*, *42*, 1053–1060, doi:10.1002/2014GL062604.

Hayes, G. P., M. W. Herman, W. D. Barnhart, K. P. Furlong, S. Riquelme, H. M. Benz, E. Bergman, S. Barrientos, P. S. Earle, and S. Samsonov (2014), Continuing megathrust earthquake potential in Chile after the 2014 Iquique earthquake, *Nature*, *512*(7514), 295–298.

Helmstetter, A., and D. Sornette (2003), Foreshocks explained by cascades of triggered seismicity, *J. Geophys. Res.*, *108*(B10), 2457, doi:10.1029/2003JB002409.

Huang, Y., L. Meng, and J.-P. Ampuero (2012), A dynamic model of the frequency-dependent rupture process of the 2011 Tohoku-Oki earthquake, *Earth Planets Space*, *64*(12), 1061–1066.

Husen, S., E. Kissling, E. Flueh, and G. Asch (1999), Accurate hypocentre determination in the seismogenic zone of the subducting Nazca Plate in northern Chile using a combined on-/offshore network, *Geophys. J. Int.*, *138*(3), 687–701.

Iida, K., D. C. Cox, and G. Pararas-Carayannis (1967), Preliminary catalog of tsunamis occurring in the Pacific ocean, Data Rep. 5, HIG-67-10, Hawaii Inst. of Geophys., Univ. Hawaii, Honolulu, Hawaii.

Jolivet, R., M. Simons, P. S. Agram, Z. Duputel, and Z. K. Shen (2015), Aseismic slip and seismogenic coupling along the central San Andreas Fault, *Geophys. Res. Lett.*, *42*, 297–306, doi:10.1002/2014GL062222.

Kato, A., K. Obara, T. Igarashi, H. Tsuruoka, S. Nakagawa, and N. Hirata (2012), Propagation of slow slip leading up to the 2011 M_W 9.0 Tohoku-Oki earthquake, *Science*, *335*(6069), 705–708.

Kelleher, J. A. (1972), Rupture zones of large South American earthquakes and some predictions, *J. Geophys. Res.*, *77*(11), 2087–2103.

Kozdon, J. E., and E. M. Dunham (2013), Rupture to the trench: Dynamic rupture simulations of the 11 March 2011 Tohoku Earthquake, *Bull. Seismol. Soc. Am.*, *103*(2B), 1275–1289.

Lay, T., H. Kanamori, C. J. Ammon, K. D. Koper, A. R. Hutko, L. Ye, H. Yue, and T. M. Rushing (2012), Depth-varying rupture properties of subduction zone megathrust faults, *J. Geophys. Res.*, *117*, B04311, doi:10.1029/2011JB009133.

Lay, T., H. Yue, E. E. Brodsky, and C. An (2014), The 1 April 2014 Iquique, Chile, M_W 8.1 earthquake rupture sequence, *Geophys. Res. Lett.*, *41*, 3818–3825, doi:10.1002/2014GL060238.

Legrand, D., B. Delouis, L. Dorbath, C. David, J. Campos, L. Marquéz, J. Thompson, and D. Comte (2007), Source parameters of the $M_w = 6.3$ Aroma crustal earthquake of July 24, 2001 (northern Chile), and its aftershock sequence, *J. South Amer. Earth Sci.*, *24*(1), 58–68.

Li, S., M. Moreno, J. Bedford, M. Rosenau, and O. Oncken (2015), Revisiting viscoelastic effects on interseismic deformation and locking degree: A case study of the Peru-North Chile subduction zone, *J. Geophys. Res. Solid Earth*, *120*, 4522–4538, doi:10.1002/2015JB011903.

Liu, C., Y. Zheng, R. Wang, and X. Xiong (2015), Kinematic rupture process of the 2014 Chile M_w 8.1 earthquake constrained by strong-motion, GPS static offsets and teleseismic data, *Geophys. J. Int.*, *202*(2), 1137–1145.

Lomnitz, C. (2004), Major earthquakes of Chile: A historical survey, 1535–1960, *Seismol. Res. Lett.*, *75*(3), 368–378.

Lüth, S. (2000), Results of wide-angle investigations and crustal structure along a traverse across the central Andes at 21 degrees south, PhD thesis, Berliner Geowissenschaftliche Abhandlungen, Inst. of Geol., Geophys. and Geoinformatics, Free Univ. of Berlin, Berlin.

Meng, L., A. Inbal, and J.-P. Ampuero (2011), A window into the complexity of the dynamic rupture of the 2011 M_w 9 Tohoku-Oki earthquake, *Geophys. Res. Lett.*, *38*, L00G07, doi:10.1029/2011GL048118.

Meng, L., H. Huang, R. Bürgmann, J.-P. Ampuero, and A. Strader (2015), Dual megathrust slip behaviors of the 2014 Iquique earthquake sequence, *Earth Planet. Sci. Lett.*, *411*, 177–187.

Metois, M., A. Socquet, C. Vigny, D. Carrizo, S. Peyrat, A. Delorme, E. Maureira, M. C. Valderas-Bermejo, and I. Ortega (2013), Revisiting the North Chile seismic gap segmentation using GPS-derived interseismic coupling, *Geophys. J. Int.*, *194*(3), 1283–1294.

Minson, S. E., M. Simons, and J. L. Beck (2013), Bayesian inversion for finite fault earthquake source models I—Theory and algorithm, *Geophys. J. Int.*, *194*(3), 1701–1726.

Motagh, M., B. Schurr, J. Anderssohn, B. Cailleau, T. R. Walter, R. Wang, and J.-P. Villotte (2010), Subduction earthquake deformation associated with 14 November 2007, M_w 7.8 Tocopilla earthquake in Chile: Results from InSAR and aftershocks, *Tectonophysics*, *490*(1-2), 60–68.

Nishenko, S. P. (1991), Circum-Pacific seismic potential: 1989–1999, *Pure Appl. Geophys.*, *135*(2), 169–259.

Noda, H., and N. Lapusta (2013), Stable creeping fault segments can become destructive as a result of dynamic weakening, *Nature*, *7433*, 518–521.

Noda, H., N. Lapusta, and H. Kanamori (2013), Comparison of average stress drop measures for ruptures with heterogeneous stress change and implications for earthquake physics, *Geophys. J. Int.*, *193*(3), 1691–1712.

Pritchard, M. E., C. Ji, and M. Simons (2006), Distribution of slip from 11 $Mw > 6$ earthquakes in the northern Chile subduction zone, *J. Geophys. Res.*, *111*, B10302, doi:10.1029/2005JB004013.

Pritchard, M. E., E. O. Norabuena, C. Ji, R. Boroschek, D. Comte, M. Simons, T. H. Dixon, and P. A. Rosen (2007), Geodetic, teleseismic, and strong motion constraints on slip from recent southern Peru subduction zone earthquakes, *J. Geophys. Res.*, *112*, B03307, doi:10.1029/2006JB004294.

Ruiz, S., M. Metois, A. Fuenzalida, J. Ruiz, F. Leyton, R. Grandin, C. Vigny, R. Madariaga, and J. Campos (2014), Intense foreshocks and a slow slip event preceded the 2014 Iquique M_w 8.1 earthquake, *Science*, *345*(6201), 1165–1169.

Schurr, B., et al. (2014), Gradual unlocking of plate boundary controlled initiation of the 2014 Iquique earthquake, *Nature*, *512*(7514), 299–302.

Witze, A. (2014), Chile quake defies expectations, *Nature*, *508*(7497), 440–441.

Yagi, Y., R. Okuwaki, B. Enescu, S. Hirano, Y. Yamagami, S. Endo, and T. Komoro (2014), Rupture process of the 2014 Iquique Chile Earthquake in relation with the foreshock activity, *Geophys. Res. Lett.*, *41*, 4201–4206, doi:10.1002/2014GL060274.